Direct Laser Synthesis and Patterning of High Entropy Oxides from Liquid Precursors

Alexander C. Castonguay[1], Nabila Nabi Nova[1], Lauren M. Dueñas[1], Shannon McGee[1], M. J. K. Lodhi[2], Yang Yang[2,3,4], Lauren D. Zarzar[1,3,5*]

1. Department of Chemistry, The Pennsylvania State University, University Park, PA 16802, USA
2. Department of Engineering Science and Mechanics, The Pennsylvania State University, University Park, PA 16802, USA
3. Materials Research Institute, The Pennsylvania State University, University Park, PA 16802, USA
4. Department of Nuclear Engineering, The Pennsylvania State University, University Park, PA 16802, USA
5. Department of Materials Science and Engineering, The Pennsylvania State University, University Park, PA 16802, USA

Correspondence to: ldz4@psu.edu

Keywords: Laser synthesis, laser patterning, nanomaterials, high entropy materials, high entropy oxides

Abstract

High entropy oxides are a class of materials distinguished by the use of configurational entropy to drive material synthesis. These materials are being examined for their exciting physiochemical properties and hold promise in numerous fields, such as chemical sensing, electronics, and catalysis. Patterning and integration of high entropy materials into devices and platforms can be difficult due to their thermal sensitivity and incompatibility with many conventional thermally-based processing techniques. In this work, we present a laser-based technique, laser-induced thermal voxels, that combines the synthesis and patterning of high entropy oxides into a single process step, thereby allowing patterning of high entropy materials directly onto substrates. As a proof-of-concept, we target the synthesis and patterning of a well-characterized rock salt-phase high entropy oxide, $(Mg_{0.2}Co_{0.2}Ni_{0.2}Cu_{0.2}Zn_{0.2})O$, as well as a spinel-phase high entropy oxide, $(Mg_{0.2}Ni_{0.2}Co_{0.2}Cu_{0.2}Zn_{0.2})Cr_2O_4$. We show through electron microscopy and X-ray analysis that the materials created are atomically homogenous and are primarily of the rock salt or spinel phase. These findings show the efficacy of laser induced thermal voxel processing for the synthesis and patterning of high entropy materials and enable new routes for integration of high entropy materials within microscale platform and devices.

Introduction

The use of configurational entropy as the driving force for the formation of single phase, multi-elemental materials has led to the discovery of dozens of new high entropy materials within the last two decades[1–6], including high entropy oxides,[4,6,7] sulfides,[8,9] and carbides[10,11]. The formation of single-phase, high entropy materials is dominated not by the enthalpy of formation, which would lead to multi-phase intermetallic compounds, but instead by the configurational entropy, which favors a solid solution of many elements. The ability to stabilize atoms in novel bonding environments imbues high entropy materials with unique and often exceptional physiochemical properties; there are high entropy oxides, for example, that have exhibited massive dielectric constants,[7] large energy storage capacities,[12] and high catalytic efficiency.[13] Given their promising properties and applications, numerous synthesis and processing techniques have been reported for high entropy materials.[1–3] However, an underlying challenge regarding the application of high entropy materials is their inherent metastability. Due to this metastability, patterning and materials integration methods that involve thermal processing steps are likely to cause phase separation and a degradation in properties. Methods that facilitate the integration

and patterning of high entropy materials in combination with other metals and oxides within devices architectures would greatly facilitate the deployment of high entropy materials in diverse applications.

The synthesis of high-entropy materials is non-trivial and requires high temperatures (typically >850 °C, material dependent) along with atomic-scale mixing of the constituent elements. The high temperature requirement is dictated by the need to make TΔS the dominant term in the Gibbs free energy, $\Delta G = \Delta H - T\Delta S$. In the first report of entropy-stabilized oxides by Rost et al., a phase transition temperature of 850 °C was found for the synthesis of the rock salt-phase of $(Mg_{0.2}Co_{0.2}Ni_{0.2}Cu_{0.2}Zn_{0.2})O$.[4] Since ball milling—a technique which does not lead to atomic scale mixing—was used to mix the constituent metal oxide powders,, the high temperature served an additional purpose of promoting enhanced diffusion and mixing of the constituent elements. Re-equilibration at 750 °C led to the reemergence of multiple phases, consistent with the fact that high entropy materials are metastable and highly sensitive to thermal processing. Solution-based syntheses, in particular laser-driven solution-based synthesis, are promising candidates to address the patterning and synthesis difficulties of high entropy materials. Solution-phase processing intrinsically mixes the constituent metal atoms on the atomic scale within the precursor, overcoming the challenges associated with slow solid-state diffusion processes; this can facilitate homogeneous mixing of the metal atoms in the resultant material, reduce the need to increase diffusion kinetics through elevated temperatures, and reduce processing times.

Laser-based solution-phase synthesis techniques, such as laser-induced hydrothermal growth[14] or laser-induced thermal voxels (LITV),[15,16] have the added benefit of being able to combine the advantages of solution-phase synthesis with the microscale, freeform patterning desired for device fabrication. LITV synthesis, for example, uses the heat generated by local absorption of a focused laser to create a "thermal voxel", which is a microscale, femtoliter volume solvothermal reactor that drives thermal decomposition of metal salt solutions into solid nanomaterials. Scanning of the laser focus is used to deposit and pattern the in-situ synthesized compounds, resulting in the simultaneous synthesis and patterning of materials from fluid precursors. This process creates high local temperatures of >1000 K at the laser focus and fast quenching rates of <1 s due to the microscale heating environment.[15,16] LITV has been demonstrated for the synthesis and patterning of a wide range of metal oxides,[15,16] reduced metals,[15–17] and graphitic carbon,[18] as well as binary and ternary metal oxides.[17,19,20] However, LITV's use in synthesizing configurationally complex or high entropy materials (e.g. mixtures containing 5 or more different metals) has not been examined. We propose that the processing environment of LITV makes it uniquely suited to high entropy material synthesis. The solution-phase nature of LITV leads to intrinsic atomic-scale mixing of the precursor elements as well as flexibility in elemental composition. In addition, the temperatures reached at the thermal voxel are theorized to be well above the critical phase transition temperature for most high entropy materials.[15-20] For example, the high entropy material $(Mg_{0.2}Co_{0.2}Ni_{0.2}Cu_{0.2}Zn_{0.2})O$, first described by Rost et al. and explored further in this work, exhibits a phase transition at 850 °C, which is within the theorized temperature range for LITV.[4,15,18]

In this letter, we explore the use of LITV processing to synthesize high entropy oxides from aqueous solutions of the constituent metal nitrate salts.[15,16] We focus primarily on the synthesis and characterization of $(Mg_{0.2}Co_{0.2}Ni_{0.2}Cu_{0.2}Zn_{0.2})O$, which is a well-characterized rock salt phase entropy-stabilized oxide first reported by Rost et al. in 2015.[4] We explore the effect of variables such as precursor concentration, precursor elemental ratio, and laser power on the high entropy oxide structure. We demonstrate that the synthesized materials exhibit nanoscale elemental homogeneity within the resolution of transmission electron microscopy, but also exhibit some small secondary peaks when examined in X-ray diffraction. The presence of these secondary peaks suggests that, while the dominant material is of a rock salt structure, some secondary phases are present. Additionally, we preliminarily investigate the synthesis of a second high entropy oxide structure, the spinel-phase $(Mg_{0.2}Ni_{0.2}Co_{0.2}Cu_{0.2}Zn_{0.2})Cr_2O_4$, demonstrating efficacy of the LITV platform toward other high entropy oxide structures. We find that, similar to the rock salt-phase, the spinel exhibits atomic-scale homogeneity

when examined in transmission electron microscopy and shows X-ray diffraction peaks indicative of a spinel-phase material. We believe that the LITV technique will be applicable to diverse high entropy material compositions and crystal structures, opening the door to the single-step integration of mixed metal oxide and single-phase high entropy materials directly into devices.

Methods

Chemicals: Nickel (II) nitrate hexahydrate >98% (Alfa Aesar), magnesium (II) nitrate hexahydrate >98% (Sigma Aldrich), copper (II) nitrate hexahydrate >98% (Arcos Organics), cobalt (II) nitrate hexahydrate >98% (Fisher Science), zinc (II) nitrate hexahydrate >99% (Sigma Aldrich), chromium (III) nitrate nonahydrate >98.5% (Alfa Aesar). All chemicals were used without further purification. 1 M precursor stock solutions were made by adding an appropriate amount of a single metal salt to a 1 mL volumetric flask, dissolving the salt with DI water, then diluting to the fill line with DI water. Mixtures were made by combining the appropriate amount of 1 M stock solutions in a small vial and shaking to ensure homogeneity.

Laser-induced thermal voxel synthesis process: The LITV setup consists of a 532 nm continuous wave variable power optically pumped semiconductor laser (Coherent Verdi G12), a set of galvanometer mirrors for beam rastering, and a nanoprecision microscope stage (Applied Scientific Instrumentation Modular Infinity Microscope) equipped with a high-power MicroSpot 50x NA 0.6 focusing objective (490-570 nm AR coated, Thorlabs) as the focusing optic (**Figure S1**). The beam was expanded to fill the back aperture of the microscope objective using a set of convex lenses (Thorlabs N-BK7-A, f=50 mm, and f=100 mm) prior to the microscope stage. We note that the 532 nm laser source wavelength was chosen due to our ease of access. Based on prior work in LITV,[15,16,19,20,21] we expect that other laser wavelengths would be compatible with LITV synthesis of high entropy oxides, provided that the deposited material sufficiently absorbs the laser in order to induce photothermal heating and local temperatures rises necessary for thermal decomposition.. Approximately 200 µL of precursor solution (variable composition based on the desired output material, see **Table S1**) was added to a borosilicate glass coverslip. Nanoparticles were synthesized and sintered to the glass by irradiating the solution with the focused laser and translating the laser across the substrate to create larger structures. The laser was rastered in a 130 µm wide line using the galvanometer mirrors at a rate of 5 pass/s, with a stage translation speed of 50 µm/s. Spacing between each line was set to 110 µm, such that there was a small 20 µm overlap between each subsequent line. Patterning of the teddy bear (**Figure 1b**) was accomplished using LabView to program the nano-precision stage. We note that we do not see flaking of the materials from the borosilicate glass substrate, but rigorous adhesion testing was not conducted for this work. We refer the reader to Kindle et al.[15] and Zarzar et al.[16] for a more in-depth discussion of the LITV process.

X-ray Diffraction: X-ray diffraction patterns were collected using a PANalytical Empyrean II with a Co Kα x-ray source (l = 1.78899 Å), a θ–θ goniometer, parallel beam optics, and point focus in reflection mode using 300 mm monocapillary incident optic. An Xcelerator PASS detector operating between 20 and 100 degrees 2θ with a step size of 0.0668 and a 150 s time per step was used. The sample was mounted on an XYZ stage.

Scanning electron microscopy (SEM) and energy-dispersive X-ray spectroscopy (EDS): SEM images were taken on a Thermo Fisher Verios G4 FEI and FEI Apreo (Materials characterization lab at Penn State) with an accelerating voltage of 20 kV. All samples were coated with ~5-6 nm of iridium before imaging to reduce charge build-up. EDS and accompanying electron micrographs were collected at 20 kV with a current of 6 nA after running beam calibration using copper tape. For all reports of compositional information, the entirety of the sample (generally ~500x500 µm) was irradiated and counts were allowed

to reach 1,000,000 to ensure accuracy. EDS analysis was done using Aztec software from Oxford Instruments, using K-series X-ray emission lines. We note that due to the significant amount of surface roughness, porosity, and overlap of the characteristic X-ray spectra of the 3d transmission metals, we expect there to be ~5% error in the reported elemental compositions of this work.

Transmission electron microscopy (TEM) and energy-dispersive X-ray (EDS) spectroscopy:

(For rock salt samples): The laser-deposited sample was scraped off the surface of the glass substrate, dispersed in an ethanol-methanol mixture, and ultrasonicated for 5-10 minutes. The particle dispersion was then drop-cast onto a lacey carbon TEM grid. High resolution TEM (HRTEM) and scanning TEM/electron dispersive spectroscopy (STEM-EDS) of the sample was performed using a FEI Talos F200X microscope (Material Characterization Laboratory, Penn State) operated at an accelerating voltage of 200 kV, offering angstrom image resolution. A high angle annular dark field (HAADF) detector was used for STEM image acquisition and EDS data collection using the Super-X EDS quad detector system at an accelerating voltage of 200kV and current of ~0.15 nA. Standardless Cliff-Lorimer quantification was performed on the deconvoluted EDS line intensity data using the Bruker Espirit software.

*(For spinel samples): S*ample was prepared using Thermo Fisher Scios-2 dual beam focused-ion-beam (FIB) system with gallium ion source. A protective platinum (pt) layer was deposited on the sample using FIB and then a lamella was lifted-out from cross section of bulk specimen and attached to TEM copper grid. Furthermore, the sample was thinned down to electron transparency using an ion beam, with successively reducing the beam current with the reduction in sample thickness. The final cleaning was done using a 2kV beam current ion beam to reduce the amorphization and the radiation damage on the sample surface. A FEI Talos F200X microscope (Material Characterization Lab, Penn State) was used to collect high resolution scanning transmission electron microscopy (HR-STEM) images, STEM energy dispersive X-ray spectroscopy (STEM-EDS) and selected area electron diffraction (SAED) pattern at an accelerating voltage of 200 kV and a current of ~0.15 nA. The STEM images were collected using high angle annular dark field imaging (HAADF) detector. STEM-EDS was acquired using SuperX energy-dispersive x-ray spectroscopy detector with high efficiency for EDS signal collection. Velox software was used for the quantification and analysis of the EDS data. Furthermore, the SAED pattern was recoded from approximately 16 μm^2 area using a SAED aperture and the pattern was indexed using single crystal software and was validated using a ratio method with SAED patterns from other spinel oxide structures (Fe_3O_4 and $MgAl_2O_4$).

Thickness measurements: Samples with thickness reported in **Table S2** were prepared by using the galvoscanning mirrors to raster repeatedly over a single line 150 µm-long line, without any accompanying stage translation. Scan rate (5 pass/s), laser power (750 mW after objective), and precursor composition ($(Mg_{0.30}Co_{0.12}Ni_{0.12}Cu_{0.20}Zn_{0.26})(NO_3)_2$) were chosen to be identical to those used to synthesize the most single-phase rock-salt HEO. The line thickness was measured using an optical profilometer (Sensofar Metrology S lynx compact 3D optimal profiler, 50x Thorlabs objective with correction collar), and an average height was taken over the entire sample. Each experiment was repeated twice, and the average values were combined to yield a single average height. For profiling the deposited single lines, the profilometer focus scanned from below to above the deposited line height to obtain a full profile.

Results and Discussion

To begin our investigation and target the synthesis of $(Mg_{0.2}Co_{0.2}Ni_{0.2}Cu_{0.2}Zn_{0.2})O$, we created an equimolar aqueous precursor solution of $(Mg_{0.2}Co_{0.2}Ni_{0.2}Cu_{0.2}Zn_{0.2})(NO_3)_2$ with a final concentration of 0.2 M for each metal (**Figure 1a**). We irradiated this solution using a 532 nm laser at 375 mW focused through a microscope objective which was scanned in a zig-zag pattern to deposit a 1 mm x 1.5 mm area on a glass substrate. (All powers reported herein are measured after the objective, see Methods and **Figure S1** for

more experimental details and laser setup). Using scanning electron microscopy (SEM) and energy dispersive X-ray spectroscopy (EDS), we found that, while the metal species appear homogenously distributed, the resulting material exhibited an elemental ratio of $Mg_{0.19}Co_{0.26}Ni_{0.28}Cu_{0.13}Zn_{0.14}$ as determined by EDS such that the elements were present in an uneven atomic ratio. This elemental composition suggests that copper and zinc were incorporated in relatively smaller amounts, whereas cobalt and nickel were incorporated in relatively larger amounts, despite the fact that all metals were present at equivalent concentrations in the precursor solution. Even with this less-than-optimal elemental ratio, we sought to understand what crystal phases were present in the material to give us a baseline reference for future samples. We conducted X-ray diffraction **(**XRD) and found a significant number of secondary peaks present in the XRD pattern for this material, suggesting the presence of multiple phases which is not indicative of a high entropy material (**Figure S2**).

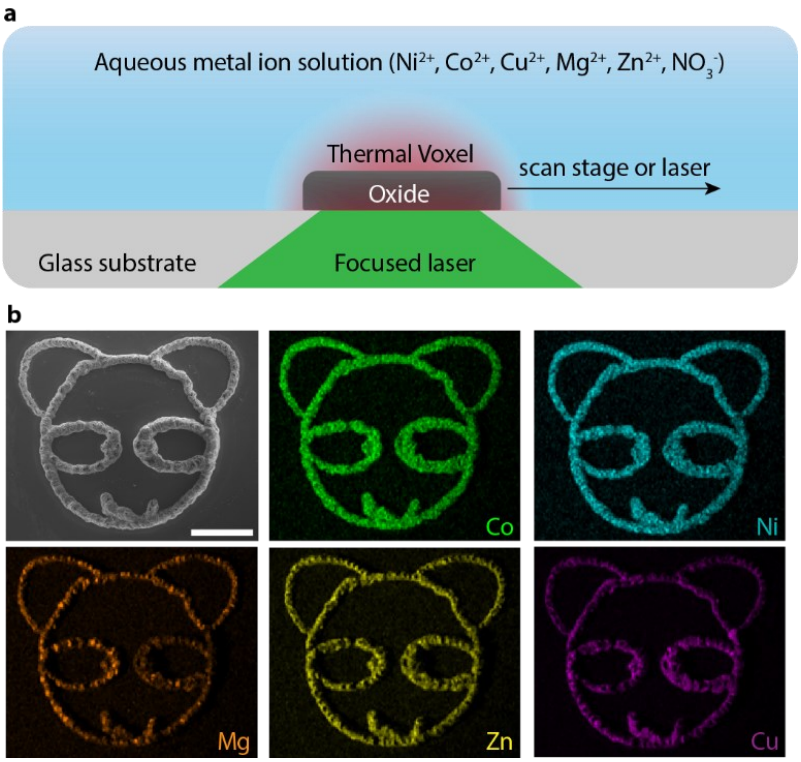

Figure 1. Process for LITV synthesis and patterning of high entropy oxides. (a) Schematic of the laser-induced thermal voxel reaction site. An aqueous mixture of Ni^{2+}, Cu^{2+}, Co^{2+}, Zn^{2+}, Mg^{2+}, and NO_3^- is thermally decomposed at the 532 nm laser focus due to highly localized heating. The resultant material contains a mixture of all five metals in an oxide lattice. The laser focus is scanned to pattern the deposited material. **(b)** EDS elemental maps and accompanying SEM of a patterned sample deposited from a $(Mg_{0.30}Co_{0.12}Ni_{0.12}Cu_{0.20}Zn_{0.26})(NO_3)_2$ aqueous precursor at 375 mW. The sample has surface roughness which could account for some of the observed macroscopic inhomogeneity of the Zn, Cu, and Mg EDS signal. The teddy bear pattern was created using a nano-precision automated stage. Scale, 1 mm.

It was clear from our initial synthesis that the relative composition of elements in the precursor and resultant deposition is not 1:1. Rost et al. showed that the configurational entropy of a system decreases rapidly as the elemental ratios deviate from equality,[4] which manifests as a marked increase in the minimum phase transition temperature for an entropy stabilized material. With this in mind, we sought to achieve a more equimolar deposition by synthesizing a series of materials from precursors with varying elemental ratios, with results from these trials shown in **Table S1**. For this precursor study, the laser power was held constant at 375 mW. We found that the precursor composition had a non-linear

effect on the resultant deposited material composition, but correlation in relative atomic ratios was present and we were able to equalize the amount of each element to a notable extent. The most equimolar deposition we achieved corresponded to an input composition of $(Mg_{0.30}Co_{0.12}Ni_{0.12}Cu_{0.20}Zn_{0.26})(NO_3)_2$, which yielded an output composition of $Mg_{0.24}Co_{0.19}Ni_{0.25}Cu_{0.17}Zn_{0.15}O$. In all samples tested, the microscale distribution of elements remained homogenous when analyzed with SEM-EDS, and the material was freely patternable using LITV (**Figure 1b**). When we examined this sample with XRD, we still found the presence of some secondary peaks centered around 2θ = 40 and 60 °. However, we did see an increase in the signal-to-noise ratio of the main rock salt peaks compared to the equimolar precursor (**Figure 2**, 375 mW sample vs. **Figure S2**).

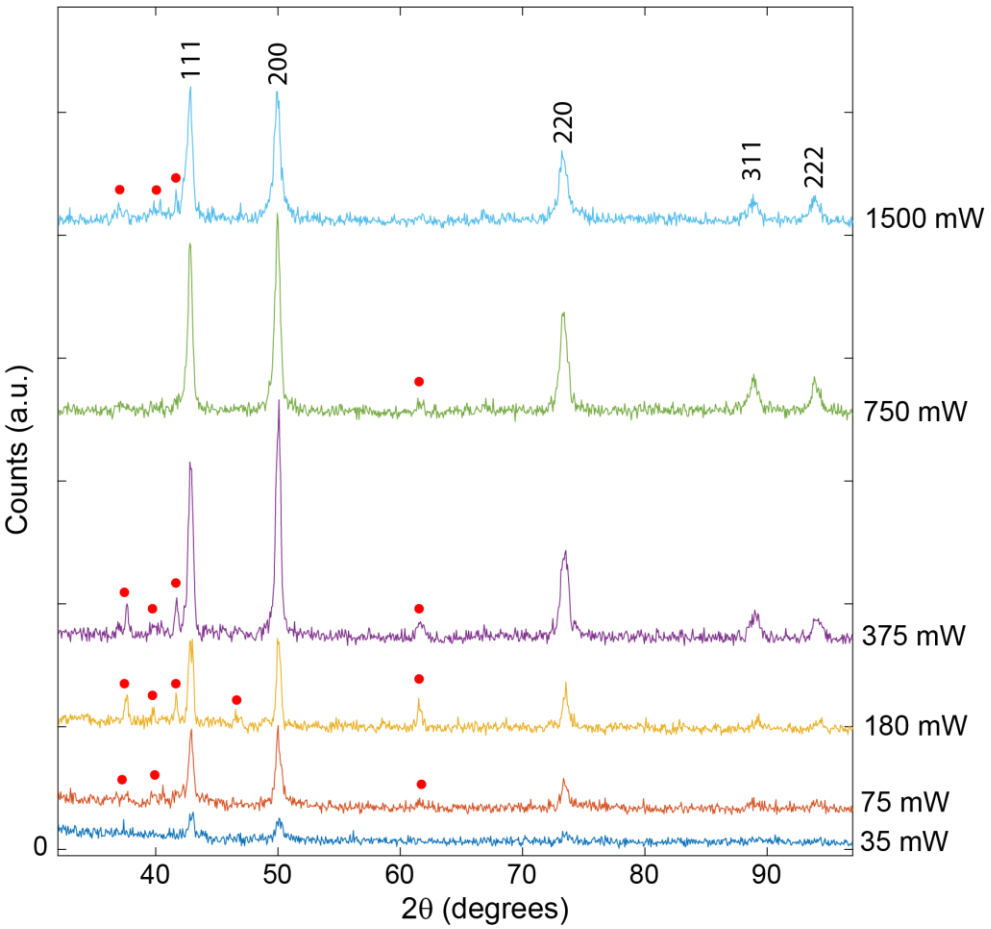

Figure 2. X-ray diffraction analysis of samples deposited from $(Mg_{0.30}Co_{0.12}Ni_{0.12}Cu_{0.20}Zn_{0.26})(NO_3)_2$ at varying laser power. Powers ranged from 37 mW to 1500 mW, measured after the microscope objective. X-ray analysis done using a Co X-ray radiation source, λ=1.78899 Å. Samples were all deposited using the same laser scanning and translation rates. Rock salt-phase Miller indices are labeled above the relevant peaks, and prominent secondary phase peaks are labeled with red dots for clarity. A decrease in the number and intensity of secondary peaks is seen as laser power increases from 37-750 mW, but a return of some secondary peaks is seen when further increasing power from 750 to 1500 mW. See supporting information for complete details on synthesis and X-ray diffraction parameters.

Having identified a more optimal high-entropy material precursor formulation, we next sought to determine if varying the laser parameters would lead to greater crystallinity and single-phase character in

the material. Changes in laser power, raster speed, and stage translation rate are all expected to have some impact on the evolution of the thermal voxel and therefore material synthesis. However, laser power is expected to have the most direct correlation to the thermal voxel temperatures based on thermal modeling studies done by Nova et al.[18] and Zarzar et al.[16] Direct measurement of the thermal voxel temperature is challenging and has not been accomplished to date; however, we postulate based on this prior work that the temperatures being reached at the thermal voxel are well above the 800-1000 ^{o}C threshold for high entropy oxide synthesis. We also observe partial melting of the borosilicate glass substrate surface which is further indicative of the high temperatures reached. Based on previous reports of high entropy oxide synthesis, we expect higher laser powers (and therefore higher temperatures) to favor single-phase high entropy oxide formation due to an increase in the entropic term of the Gibbs free energy. To study this potential laser power-crystallinity correlation, we systematically varied the laser power from 37 mW to 1500 mW using the optimized precursor found previously, aqueous $(Mg_{0.30}Co_{0.12}Ni_{0.12}Cu_{0.20}Zn_{0.26})(NO_3)_2$. We then analyzed each of the resultant materials using XRD, with results shown in **Figure 2**. We found that from 37-750 mW, increasing laser power led to a reduction in the number and intensity of secondary phases and an increase in the intensity of the rock salt peaks, which supports our initial hypothesis that higher laser powers would favor single-phase formation. However, when the laser power was further increased from 750 to 1500 mW, we saw a return of secondary peaks centered around 2θ=40° and the relative intensity of the (111) and (200) rock salt peaks decreased. We note that there was minimal change to the observed elemental composition at varying laser powers based on comparison of samples deposited at 375 mW ($Mg_{0.24}Co_{0.19}Ni_{0.25}Cu_{0.17}Zn_{0.15}O$) and 750 mW ($Mg_{0.21}Co_{0.20}Ni_{0.25}Cu_{0.19}Zn_{0.15}O$).

Since high entropy materials are inherently metastable and have a reversible phase transition if heated below their phase transition temperature, one explanation for the return of secondary peaks at the highest laser powers may be from reheating of previously-deposited material near the laser voxel. The temperature around the thermal voxel decreases rapidly as a function of distance, but with increased laser power, a larger microscale area around the voxel is heated to appreciable temperatures. During synthesis, the laser is passed back and forth across the glass substrate repeatedly, and as such the increased size of the heated zone around the thermal voxel for higher laser powers may anneal nearby high entropy oxide grains below their phase transition temperature, resulting in the emergence of secondary phases. Based on the XRD and EDS data in **Figure 1** and **Figure 2**, we chose to further characterize the material deposited at 750 mW, found to have an elemental composition of $Mg_{0.21}Co_{0.20}Ni_{0.25}Cu_{0.19}Zn_{0.15}O$ and few secondary peaks, suggesting that while some crystalline secondary phases are present, the predominant material is of a rock salt structure.

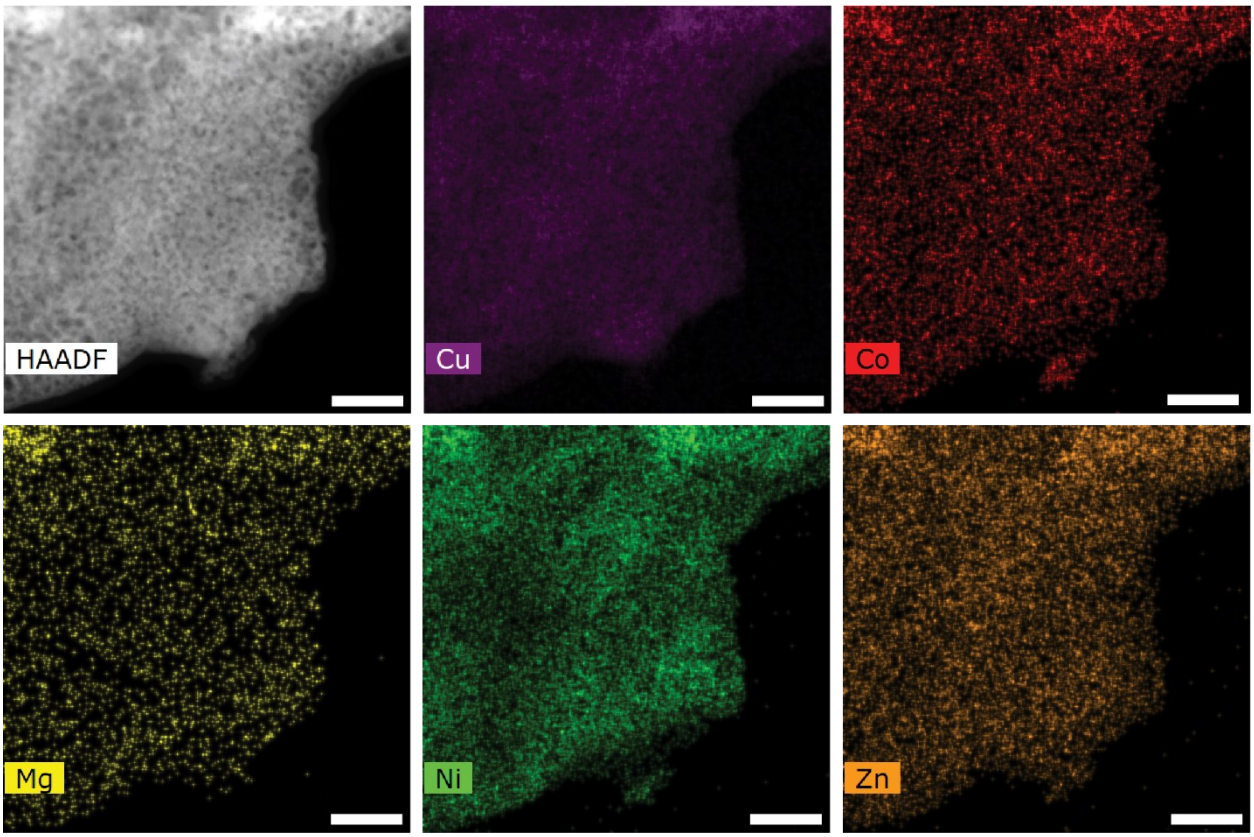

Figure 3. TEM-EDS of material deposited from $(Mg_{0.30}Co_{0.12}Ni_{0.12}Cu_{0.20}Zn_{0.26})(NO_3)_2$ at 750 mW. High-angle annular darkfield transmission electron micrograph with corresponding EDS maps of material created using a 750 mW deposition from the aqueous precursor $(Mg_{0.30}Co_{0.12}Ni_{0.12}Cu_{0.20}Zn_{0.26})(NO_3)_2$. EDS shows an even distribution of all five metal ions throughout the material at the nanoscale. Scale bars 10 nm.

To further characterize the phase and morphology of the material synthesized at 750 mW, and to identify if the rock salt phase seen in XRD of the 750 mW sample came from a multi-element high entropy material, we conducted profilometry, SEM, and high-resolution transmission electron microscopy (HRTEM) with accompanying EDS (**Figure 3** and **Figure S3**). Our goal in this analysis was to observe the morphological characteristics (such as thickness and surface roughness) and elemental distribution in the material at a higher resolution to help determine if there was any observable phase separation or aggregation of a particular element. We found the samples were composed of a rough surface of small nanoparticle aggregates, on the order of 10s-100s of nm (SEM, **Figure S3**), and that all five metals appeared to be well distributed throughout the sample at nanometer resolution, suggesting that the rock salt phase seen in XRD is coming from a high entropy material containing all five metal elements (**Figure 3**). We also found that the samples plateaued at approximately 20 µm in thickness after 5 seconds of repeated laser scanning over the same area at 5 pass/s (**Table S2**). Using HRTEM, we were able to observe and measure the d-spacing of select grains within the sample, which matched to the (111) and (200) rock salt planes (**Figure S4**). Although the small secondary peaks visible in XRD indicate that these initial attempts at patterning high entropy materials using LITV are not completely single-phase, we believe, based on the HRTEM and the elemental mapping shown in **Figure 3** in addition to the XRD patterns, that the predominant material present in the 750 mW deposition is of the high entropy rock salt phase $(Mg_{0.2}Co_{0.2}Ni_{0.2}Cu_{0.2}Zn_{0.2})O$ initially described by Rost *et al*.[4]

We initially hypothesized that LITV would be generally applicable to high entropy oxide synthesis, of which there are numerous different possible oxides. Based on the nominal success of the synthesis of $Mg_{0.19}Co_{0.24}Ni_{0.26}Cu_{0.19}Zn_{0.12}O$ we set out to determine if LITV could create other high entropy oxide phases. In our preliminary effort, we targeted a high entropy spinel composition, $(Mg_{0.2}Ni_{0.2}Co_{0.2}Cu_{0.2}Zn_{0.2})Cr_2O_4$, following the same process of precursor compositional variation followed by XRD and TEM-EDS analysis. We found that a precursor composition of 0.1 M each of $Mg(NO_3)_2$, $Ni(NO_3)_2$, $Co(NO_3)_2$, $Cu(NO_3)_2$, and $Zn(NO_3)_2$, with 1 M $Cr(NO_3)_3$ deposited at 435 mW yielded an overall material composition of $(Mg_{0.15}Ni_{0.21}Co_{0.27}Cu_{0.21}Zn_{0.39})Cr_{1.75}O_x$ with elements distributed homogenously throughout the material at the nanoscale and an XRD pattern consisting of spinel-phase peaks (**Figure 4**). A cross-section of this sample was also analyzed using TEM-EDS to determine if the elemental homogeneity persisted throughout the depth of the material (**Figure S5**). We again found that there was no significant elemental segregation, and the sample appeared homogenous. This cross-sectional analysis also revealed significant macropores present throughout the material, on the order of 1 µm in size. This, along with the surface roughness seen in SEM, suggests that these materials may have a high accessible surface area which could be advantageous for applications including catalysis and sensing. Oxygen content was not analyzed directly, and the signal-to-noise ratio of the X-ray pattern is low, suggesting that the material may have significant amorphous or disordered character, but the presence of the main spinel-phase peaks and the absence of any visible predominant secondary peaks points to the successful synthesis of a spinel-phase high entropy material. We note that only one of the constituent single metals are of a spinel phase, cobalt (II,III) oxide (Co_3O_4), such that the spinel phase seen in the XRD pattern is expected to result from a multi-metal oxide. The significant deviation from optimal elemental composition, seen most prominently with Zn and Cr, may contribute to the low XRD signal. To corroborate the spinel-phase peaks seen in XRD, we conducted selected area electron diffraction (SAED) as a means of obtaining more complete phase characterization. The SAED data, shown in **Figure S6**, supports the XRD data with only spinel-phase diffraction rings observed, suggesting that this material is a fully single-phase high entropy oxide. This result, in conjunction with the nearly single-phase rock-salt material described above, demonstrate the efficacy of LITV for the synthesis and patterning of high entropy oxides, with the potential to pattern other compositions and crystal structures than those reported in this work.

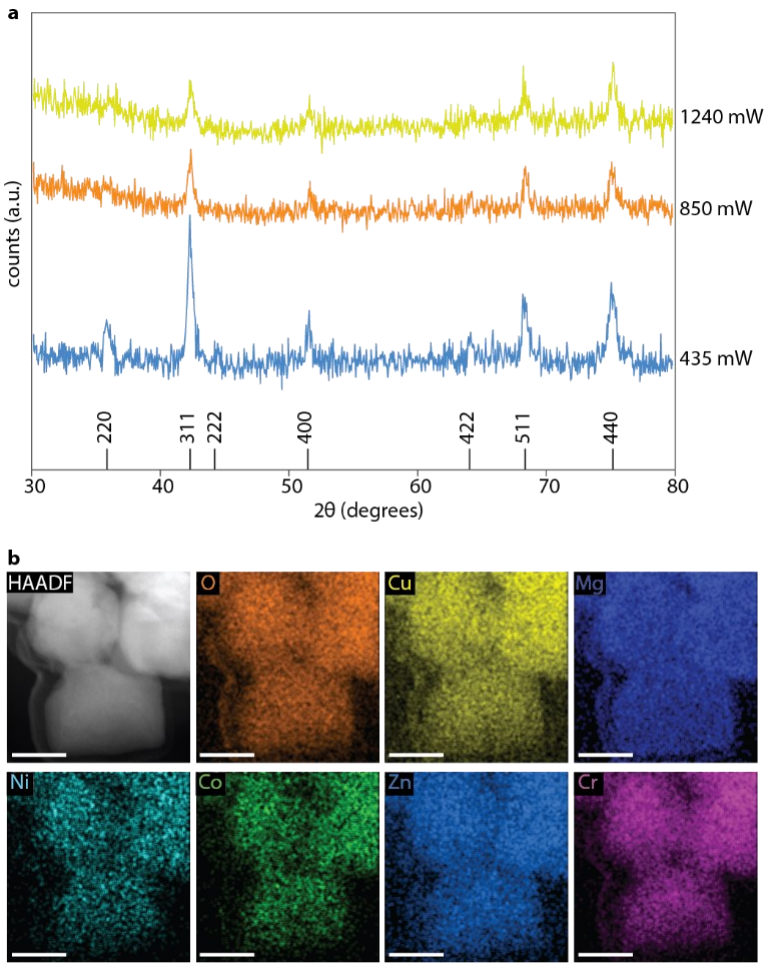

Figure 4. XRD and TEM-EDS analysis of LITV-synthesized spinel-phase high entropy oxide, $(Mg_{0.15}Ni_{0.21}Co_{0.27}Cu_{0.21}Zn_{0.39})Cr_{1.75}O_x$. Samples were prepared from an aqueous mixture of 0.1 M each $Mg(NO_3)_2$, $Ni(NO_3)_2$, $Co(NO_3)_2$, $Cu(NO_3)_2$, and $Zn(NO_3)_2$, with 1 M $Cr(NO_3)_3$. **(a)** XRD analysis of samples deposited at varying laser power. XRD patterns show that crystallinity decreases as laser power is increased from 435-1240 mW. While the signal to noise ratio is low, the only observable peaks are those from a spinel-phase crystal. **(b)** TEM-EDS analysis of the sample deposited at 435 mW shows an even distribution of each metal throughout the material. Scale bars 50 nm.

Conclusion

In this work, we presented the use of a thermally driven direct laser writing method for the simultaneous synthesis and patterning of two high entropy oxides: the rock salt-phase $(Mg_{0.2}Co_{0.2}Ni_{0.2}Cu_{0.2}Zn_{0.2})O$ and the spinel-phase $(Mg_{0.2}Ni_{0.2}Co_{0.2}Cu_{0.2}Zn_{0.2})Cr_2O_4$. No observable secondary phases in the spinel material were found, while a small percentage of secondary phases in the X-ray pattern of the rock salt structure were observed. Based on a combination HRTEM, SAED, XRD, and elemental analysis, we find that the predominant phases are spinel or rock salt. We also observe atomic-scale elemental homogeneity in both samples, consistent with high entropy oxides. We analyze the effects of laser power and precursor composition on the resultant material's phase and elemental homogeneity and find that there is some control over phase structure through variation of laser power, with mid-range laser powers of 750 mW (rock salt) or 435 mW (spinel) focused to a microscale area leading to the most single-phase material and both lower and higher laser powers exhibiting increased amounts of secondary phases. We also found that, while there was some correlation between the elemental ratios of the

precursor and the resulting deposition, the effects of varying precursor composition were non-linear and therefore difficult to predict. The contribution of this work lies in the potential to pattern high entropy materials directly from fluid precursors onto microscale devices. Previous work using the LITV technique has shown that patterns with line width resolution on the scale of 1 micron can be achieved,[16] which makes the method broadly applicable to microfabrication or microelectronic applications. We hope that this technique will give greater control over the integration of these promising high entropy materials into microscale devices, such as sensors or catalyst platforms, where their unique properties can be harnessed.

Acknowledgements. L.Z, A.C., N.N., S.M. and L.D. acknowledge financial support from the NSF (CMMI-2046819), the Sloan Research Fellowship (FG-2020-12707), the Packard Foundation (2019-69664), and seed funding from the Institutes for Energy and the Environment at Penn State University. M.J.K.L. and Y.Y. acknowledge the support from seed funding from the Institutes for Energy and the Environment at Penn State University.

Data availability statement. The data that support the findings of this study that are not already included within the article or supporting information are available upon request from the authors.

References

(1) Albedwawi, S. H.; Aljaberi, A.; Haidemenopoulos, G. N.; Polychronopoulou, K. High Entropy Oxides-Exploring a Paradigm of Promising Catalysts : A Review. *Mater. Des.* **2021**, *202*, 109534. https://doi.org/10.1016/j.matdes.2021.109534.

(2) Tomboc, G. M.; Zhang, X.; Choi, S.; Kim, D.; Lee, L. Y. S.; Lee, K. Stabilization, Characterization, and Electrochemical Applications of High-Entropy Oxides: Critical Assessment of Crystal Phase–Properties Relationship. *Adv. Funct. Mater.* **2022**, *32* (43). https://doi.org/10.1002/adfm.202205142.

(3) Brahlek, M.; Gazda, M.; Keppens, V.; Mazza, A. R.; McCormack, S. J.; Mielewczyk-Gryń, A.; Musico, B.; Page, K.; Rost, C. M.; Sinnott, S. B.; et al. What Is in a Name: Defining "High Entropy" Oxides. *APL Mater.* **2022**, *10* (11), 110902. https://doi.org/10.1063/5.0122727.

(4) Rost, C. M.; Sachet, E.; Borman, T.; Moballegh, A.; Dickey, E. C.; Hou, D.; Jones, J. L.; Curtarolo, S.; Maria, J. P. Entropy-Stabilized Oxides. *Nat. Commun.* **2015**, *6*, 1–8. https://doi.org/10.1038/ncomms9485.

(5) Yeh, J. W.; Chen, S. K.; Lin, S. J.; Gan, J. Y.; Chin, T. S.; Shun, T. T.; Tsau, C. H.; Chang, S. Y. Nanostructured High-Entropy Alloys with Multiple Principal Elements: Novel Alloy Design Concepts and Outcomes. *Adv. Eng. Mater.* **2004**, *6* (5), 299–303. https://doi.org/10.1002/adem.200300567.

(6) Sarkar, A.; Wang, Q.; Schiele, A.; Chellali, M. R.; Bhattacharya, S. S.; Wang, D.; Brezesinski, T.; Hahn, H.; Velasco, L.; Breitung, B. High-Entropy Oxides: Fundamental Aspects and Electrochemical Properties. *Adv. Mater.* **2019**, *31* (26). https://doi.org/10.1002/adma.201806236.

(7) Bérardan, D.; Franger, S.; Dragoe, D.; Meena, A. K.; Dragoe, N. Colossal Dielectric Constant in High Entropy Oxides. *Phys. Status Solidi - Rapid Res. Lett.* **2016**, *10* (4), 328–333. https://doi.org/10.1002/pssr.201600043.

(8) Cui, M.; Yang, C.; Li, B.; Dong, Q.; Wu, M.; Hwang, S.; Xie, H.; Wang, X.; Wang, G.; Hu, L. High-Entropy Metal Sulfide Nanoparticles Promise High-Performance Oxygen Evolution Reaction. *Adv. Energy Mater.* **2021**, *11* (3), 1–8. https://doi.org/10.1002/aenm.202002887.

(9) Lin, L.; Wang, K.; Sarkar, A.; Njel, C.; Karkera, G.; Wang, Q.; Azmi, R.; Fichtner, M.; Hahn, H.; Schweidler, S.; et al. High-Entropy Sulfides as Electrode Materials for Li-Ion Batteries. *Adv. Energy Mater.* **2022**, *12* (8). https://doi.org/10.1002/aenm.202103090.

(10) Sarker, P.; Harrington, T.; Toher, C.; Oses, C.; Samiee, M.; Maria, J. P.; Brenner, D. W.; Vecchio, K. S.; Curtarolo, S. High-Entropy High-Hardness Metal Carbides Discovered by Entropy Descriptors. *Nat. Commun.* **2018**, *9* (1), 1–10. https://doi.org/10.1038/s41467-018-07160-7.

(11) Zhou, J.; Zhang, J.; Zhang, F.; Niu, B.; Lei, L.; Wang, W. High-Entropy Carbide: A Novel Class of Multicomponent Ceramics. *Ceram. Int.* **2018**, *44* (17), 22014–22018. https://doi.org/10.1016/j.ceramint.2018.08.100.

(12) Sarkar, A.; Velasco, L.; Wang, D.; Wang, Q.; Talasila, G.; de Biasi, L.; Kübel, C.; Brezesinski, T.; Bhattacharya, S. S.; Hahn, H.; et al. High Entropy Oxides for Reversible Energy Storage. *Nat. Commun.* **2018**, *9* (1). https://doi.org/10.1038/s41467-018-05774-5.

(13) Chen, H.; Fu, J.; Zhang, P.; Peng, H.; Abney, C. W.; Jie, K.; Liu, X.; Chi, M.; Dai, S. Entropy-Stabilized Metal Oxide Solid Solutions as CO Oxidation Catalysts with High-Temperature Stability. *J. Mater. Chem. A* **2018**, *6* (24), 11129–11133. https://doi.org/10.1039/c8ta01772g.

(14) Yeo, J.; Hong, S.; Kim, G.; Lee, H.; Suh, Y. D.; Park, I.; Grigoropoulos, C. P.; Ko, S. H. Laser-Induced Hydrothermal Growth of Heterogeneous Metal-Oxide Nanowire on Flexible Substrate by Laser Absorption Layer Design. *ACS Nano* **2015**, *9* (6), 6059–6068. https://doi.org/10.1021/acsnano.5b01125.

(15) Kindle, C.; Castonguay, A.; McGee, S.; Tomko, J. A.; Hopkins, P. E.; Zarzar, L. D. Direct Laser Writing from Aqueous Precursors for Nano to Microscale Topographical Control, Integration, and Synthesis of Nanocrystalline Mixed Metal Oxides. *ACS Appl. Nano Mater.* **2019**, *2*, 2581–2586. https://doi.org/10.1021/acsanm.9b00360.

(16) Zarzar, L. D.; Swartzentruber, B. S.; Donovan, B. F.; Hopkins, P. E.; Kaehr, B. Using Laser-Induced Thermal Voxels to Pattern Diverse Materials at the Solid-Liquid Interface. *ACS Appl. Mater. Interfaces* **2016**, *8* (33), 21134–21139. https://doi.org/10.1021/acsami.6b06625.

(17) McGee, S.; Fest, A.; Chandler, C.; Nova, N. N.; Lei, Y.; Goff, J.; Sinnott, S. B.; Dabo, I.; Terrones, M.; Zarzar, L. D. Direct Laser Writing of Multimetal Bifunctional Catalysts for Overall Water Splitting. *ACS Appl. Energy Mater.* **2023**. https://doi.org/10.1021/acsaem.2c03973.

(18) Nova, N. N.; Zarzar, L. D. Direct Laser Writing of Graphitic Carbon from Liquid Precursors. *Chem. Mater.* **2022**, *34* (10), 4602–4612. https://doi.org/10.1021/acs.chemmater.2c00467.

(19) Castonguay, A. C.; Yi, N.; Li, B.; Zhao, J.; Li, H.; Gao, Y.; Nova, N. N.; Tiwari, N.; Zarzar, L. D.; Cheng, H. Direct Laser Writing of Microscale Metal Oxide Gas Sensors from Liquid Precursors. *ACS Appl. Mater. Interfaces* **2022**, *14* (24), 28163–28173. https://doi.org/10.1021/acsami.2c03561.

(20) McGee, S.; Lei, Y.; Goff, J.; Wilkinson, C.; Nova, N. N.; Kindle, C. M.; Zhang, F.; Fujisawa, K.; Dimitrov, E.; Sinnott, S. B.; et al. Single-Step Direct Laser Writing of Multimetal Oxygen Evolution Catalysts from Liquid Precursors. *ACS Nano* **2021**, *15* (6), 9796–9807. https://doi.org/10.1021/acsnano.1c00650.

(21) Zarzar, L. D.; Swartzentruber, B. S.; Harper, J. C.; Dunphy, D. R.; Brinker, C. J.; Aizenberg, J.; Kaehr, B. Multiphoton Lithography of Nanocrystalline Platinum and Palladium for Site-Specific Catalysis in 3D Microenvironments. *J. Am. Chem. Soc.* **2012**, *134* (9), 4007–4010. https://doi.org/10.1021/ja211602t.